AGU PUBLICATIONS

JGR

Journal of Geophysical Research: Oceans

RESEARCH ARTICLE

10.1002/2016JC012283

Special Section:
Atmosphere-ice-ocean-ecosystem Processes in a Thinner Arctic Sea Ice Regime: the Norwegian Young Sea ICE Cruise 2015 (N-ICE2015)

Turbulent heat and momentum fluxes in the upper ocean under Arctic sea ice

Algot K. Peterson[1,2], Ilker Fer[1,2], Miles G. McPhee[3], and Achim Randelhoff[4,5]

[1]Geophysical Institute, University of Bergen, Bergen, Norway, [2]Bjerknes Centre for Climate Research, Bergen, Norway, [3]McPhee Research Company, Naches, Washington, USA, [4]Institute for Arctic and Marine Biology, UiT, Arctic University of Norway, Tromsø, Norway, [5]Norwegian Polar Institute, Tromsø, Norway

Abstract We report observations of heat and momentum fluxes measured in the ice-ocean boundary layer from four drift stations between January and June 2015, covering from the typical Arctic basin conditions in the Nansen Basin to energetic spots of interaction with the warm Atlantic Water branches near the Yermak Plateau and over the North Spitsbergen slope. A wide range of oceanic turbulent heat flux values are observed, reflecting the variations in space and time over the five month duration of the experiment. Oceanic heat flux is weakly positive in winter over the Nansen Basin during quiescent conditions, increasing by an order of magnitude during storm events. An event of local upwelling and mixing in the winter-time Nansen basin highlights the importance of individual events. Spring-time drift is confined to the Yermak Plateau and its slopes, where vertical mixing is enhanced. Wind events cause an approximate doubling of oceanic heat fluxes compared to calm periods. In June, melting conditions near the ice edge lead to heat fluxes of O(100 W m^{-2}). The combination of wind forcing with shallow Atlantic Water layer and proximity to open waters leads to maximum heat fluxes reaching 367 W m^{-2}, concurrent with rapid melting. Observed ocean-to-ice heat fluxes agree well with those estimated from a bulk parameterization except when accumulated freshwater from sea ice melt in spring probably causes the bulk formula to overestimate the oceanic heat flux.

Key Points:
- Unique winter and spring measurements of under-ice turbulence characteristics in the Eastern Arctic
- Winter oceanic turbulent heat flux toward ice is O(1) W m^{-2} in deep Arctic
- Under-ice heat fluxes are O(100) W m^{-2} near Atlantic Water pathways

Correspondence to:
A. K. Peterson,
algot@uib.no

Citation:
Peterson, A. K., I. Fer, M. G. McPhee, and A. Randelhoff (2017), Turbulent heat and momentum fluxes in the upper ocean under Arctic sea ice, *J. Geophys. Res. Oceans*, *122*, 1439–1456, doi:10.1002/2016JC012283.

Received 26 AUG 2016
Accepted 24 JAN 2017
Accepted article online 31 JAN 2017
Published online 25 FEB 2017

1. Introduction

Ocean heat is a key factor in the heat budget of Arctic sea ice, and small changes in oceanic heat transport can have a substantial influence on the sea ice cover [*Carmack et al.*, 2015]. Summer sea ice extent is declining increasingly fast [*Serreze and Stroeve*, 2015], and what was once a thick, perennial ice cover has now been replaced by thinner first-year ice [*Krishfield et al.*, 2014; *Lindsay and Schweiger*, 2015]. The Arctic seems to have shifted to a new normal state [*Jeffries et al.*, 2013], and we are facing essentially ice-free summers [*Stroeve et al.*, 2012]. With a seasonally ice-free Arctic, a stronger seasonality in heat exchange between the upper ocean and ice/atmosphere is expected [*Tietsche et al.*, 2011]. A reduced ice cover may lead to increased energy input from direct wind forcing to the upper ocean [*Rainville et al.*, 2011].

In the interior Arctic, turbulent heat exchange is limited by the cold halocline layer [*Fer*, 2009], and heat transfer is dominated by individual events [*Fer*, 2014]. The warm boundary currents in the Eastern Arctic, however, are associated with turbulent oceanic fluxes elevated by up to two orders of magnitude [*Sirevaag and Fer*, 2009]. The marginal ice zone (MIZ) is often located over the Yermak Plateau (YP), a manifestation of large oceanic heat loss to melting ice along the path of Atlantic Water (AW) north of Svalbard. Although large regional and seasonal variability in ocean heat flux has been observed, the contribution and importance of the oceanic heat for the variability of the sea ice cover is still not accurately quantified [*Carmack et al.*, 2015].

A few major experiments have shed light on the heat budget of the Arctic sea ice cover. From the 1975 Arctic Ice Dynamics Joint Experiment (AIDJEX), *Maykut and McPhee* [1995] demonstrated the strong seasonal cycle in oceanic heat flux and found solar radiation to be the major source of upper ocean heat in the central Arctic. During the yearlong drift of SHEBA (Surface Heat Budget of the Arctic) over the western Arctic, ocean-to-ice heat flux was low to moderate (~3.5 W m^{-2}) in the first parts of the record, reflecting

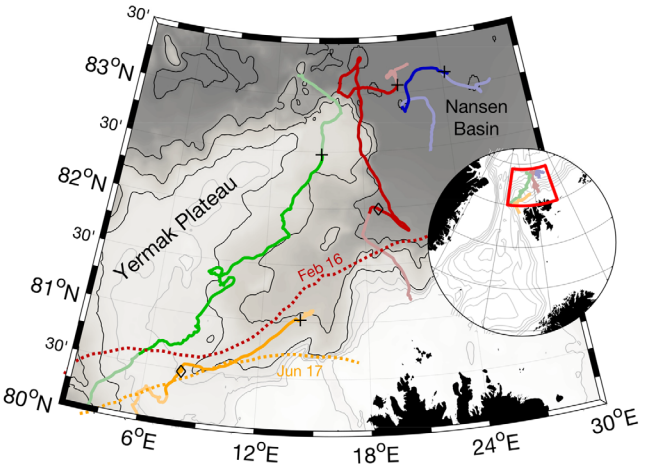

Figure 1. Map of the study area, north of Svalbard, as shown in the inset. Drift track is shown in faint colors, and track covered by TIC sampling in clear colors. Each color represents one drift, and is consistent with following figures. Crosses mark the start of TIC sampling. Bathymetry is from ETOPO-1, with isobaths at 1000 m intervals in black, and at 250 m intervals for depths shallower than 1000 m in gray. Lines for 50% sea ice concentration are shown for two dates (marked by diamonds on the track), based on satellite data acquired from the Norwegian Meteorological Institute.

variations in bathymetry and stratification. Solar heating of the upper ocean was the dominant heat source during the summer part of the drift [*Shaw et al.*, 2009]. *Hudson et al.* [2013] observed significant contribution of oceanic heat flux to the energy budget of melting first-year ice in the Nansen Basin. In spring and summer when the radiation forcing is strong, it is challenging to quantify the oceanic contribution to the energy balance. In winter, on the other hand, when the sole source of heat is the oceanic heat, it is possible to quantify the vertical flux of heat from the ocean interior.

Winter observations in the Arctic are sparse, and the most notable exceptions, AIDJEX and SHEBA, were both from the central western Arctic. More typical field campaigns in the Arctic are drift stations in the marginal ice zone in spring, lasting a few days or less [*Sirevaag and Fer*, 2009]. In recent years, autonomous measurement systems have proven useful in for long-term measurements of Arctic Ocean momentum and heat fluxes in the Canada Basin [*Cole et al.*, 2014; *Gallaher et al.*, 2016] and along the transpolar drift [*Shaw et al.*, 2008; *Stanton et al.*, 2012].

Here we present approximately two months duration measurements of directly measured heat and momentum fluxes, sampled from four consecutive drift stations north of Svalbard, spanning from January to June 2015. The drift trajectories cover the deep Nansen Basin, the shelf break, and the YP. In the Nansen Basin, conditions are typical of the central Arctic, while the MIZ and the presence of the inflowing warm AW dominate when the drift is over topography. The main purpose of this paper is to describe the under-ice boundary layer conditions encountered during the drifts. Furthermore, we assess the relative importance of oceanic heat flux in winter versus spring, and contrast measurements from the Arctic basins versus over the boundary current and topographic features.

2. General Description of the Experiment

2.1. Ice Camp Floes

As a part of the Norwegian Young Sea Ice Cruise project (N-ICE2015) [*Granskog et al.*, 2016], the research vessel (RV) Lance conducted multiple drifts from January through June 2015 in the sea ice north of Svalbard. A total of four subsequent ice camps were supported by the RV Lance (Figure 1), hereinafter referred to as Floes 1–4. Floes 1 and 2 were typically confined to the deep Nansen Basin, starting their southward drift from approximately 83°N. Floe 3 drifted southwest over the eastern flanks and then across the Yermak Plateau (YP), whereas Floe 4 started its drift closer to the continental slope north of Spitsbergen and proceeded over to the southern parts of the YP. Durations of the four ice floes were 38, 23, 49, and 15 days, respectively, 126 days in total. The first two floes can be considered winter conditions, Floe 3 covers spring and Floe 4 was early summer conditions. Floe 1 drifted in complete darkness, and on 1 March, the sun rose after four and a half months of polar night at 83°N. Five weeks after the first sunrise, on 5 April, was the onset of midnight sun.

At each floe, a turbulence instrument cluster (TIC, section 3.1) measurement system was established. The measurements from the TICs constitute the main data set of this study. The details of the TIC coverage for each floe are given in Table 1 and highlighted in colors in Figures 1 and 2.

Table 1. TIC Deployment Details for the Four Floes[a]

	Start Date	Start Position	End Date	End Position	Duration (h)	Distance (km)
Floe 1	Jan 24	83°4′N, 20°43′E	Feb 17	81°57′N, 018°8′E	524	349
Floe 2	Mar 4	83°8′N, 24°14′E	Mar 15	82° 53′N, 020°55′E	155	89
Floe 3	Apr 26	82°29′N, 15°6′E	Jun 2	80°34′N, 005°32′E	892	406
Floe 4	Jun 10	81°1′N, 14°10′E	Jun 19	80°15′N, 007°21′E	200	175

[a]Date is in 2015. Duration is length of TIC data coverage, prior to quality screening.

2.2. Environmental Conditions

In the following, storms are defined as by L. Cohen *et al.* (Meteorological conditions during the Norwegian Young Sea Ice (N-ICE) experiment, submitted to *Journal of Geophysical Research*, 2017), and are indicated by horizontal bars in Figure 3b. Start and end of storms correspond to periods when the 10 min averaged wind speed at 10 m height (U_{10m}) was greater than 8 m s^{-1} for more than 3 h, with no interruptions exceeding 1 h. A storm is classified as "major" when the rate of pressure decrease exceeds 5 hPa in 6 h. Wind measurements from the on-ice weather-mast are supplemented by ship-based measurements, adjusted to the 10 m measurement height [*Hudson et al.*, 2015; L. Cohen *et al.*, submitted manuscript, 2017].

Drift velocity, U_{ice}, is calculated from the ship's GPS position (Figure 3c). U_{ice} includes the signature of inertial and tidal oscillations. Because the near-surface water column typically oscillates approximately in phase with the ice, the instantaneous U_{ice}, or the shear between the ice drift and measured ice-relative current in the surface layer, is not representative of turbulence production. Therefore, following *McPhee* [1988], we also present the filtered (demodulated with diurnal and semidiurnal, approximately inertial, frequencies) drift speed together with the average measured ice-relative current at 1 m below the ice undersurface.

The drift of Floe 1 was mostly over the abyssal Nansen Basin. Winds measured at 10 m height were modest (5.1 m s^{-1} average) and ice drift slow (8 cm s^{-1}) during the first 10 days of the measurements. On 3 February, a storm pushed the ice northward, compacting the ice for 2 days, before the wind turned, and flushed the floe southward until the end of the storm on 9 February. During the 5.4 day longstorm (mean $U_{10m} = 12$ m s^{-1}, $U_{ice} = 28$ cm s^{-1}), the floe traveled 136 km. For comparison, total drift over the 10.5 days prior to the storm was 72 km. During the swift southward drift, the floe passed the eastern tip of the YP, with water depths shoaling to 1600 m before entering deeper water between the plateau and the Svalbard shelf (Sofia Deep). In mid-February, another storm brought strong winds and high drift speed and led the floe further south. The floe broke up, and TIC logging terminated before the floe drifted onto the Svalbard shelf.

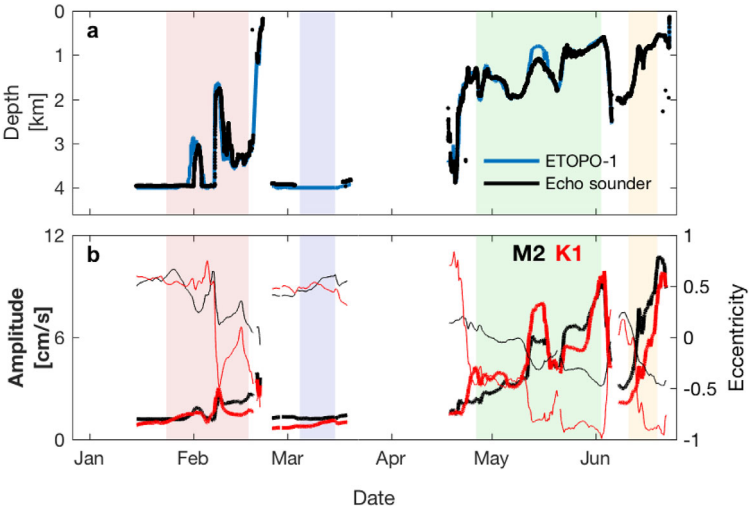

Figure 2. Time series of water depth and tidal currents. (a) Water depth from the ship's echo sounder (blue) and ETOPO-1 bathymetry (black). During most of Floe 2 the echo sounder was covered by ice. (b) Tidal parameters from AOTIM-5 [*Padman and Erofeeva*, 2004] along the ship track; major tidal ellipse amplitudes and eccentricity (thin line) for M_2 (black) and K_1 (red) tidal constituents. Shading indicates data coverage of the TIC, colors following Figure 1.

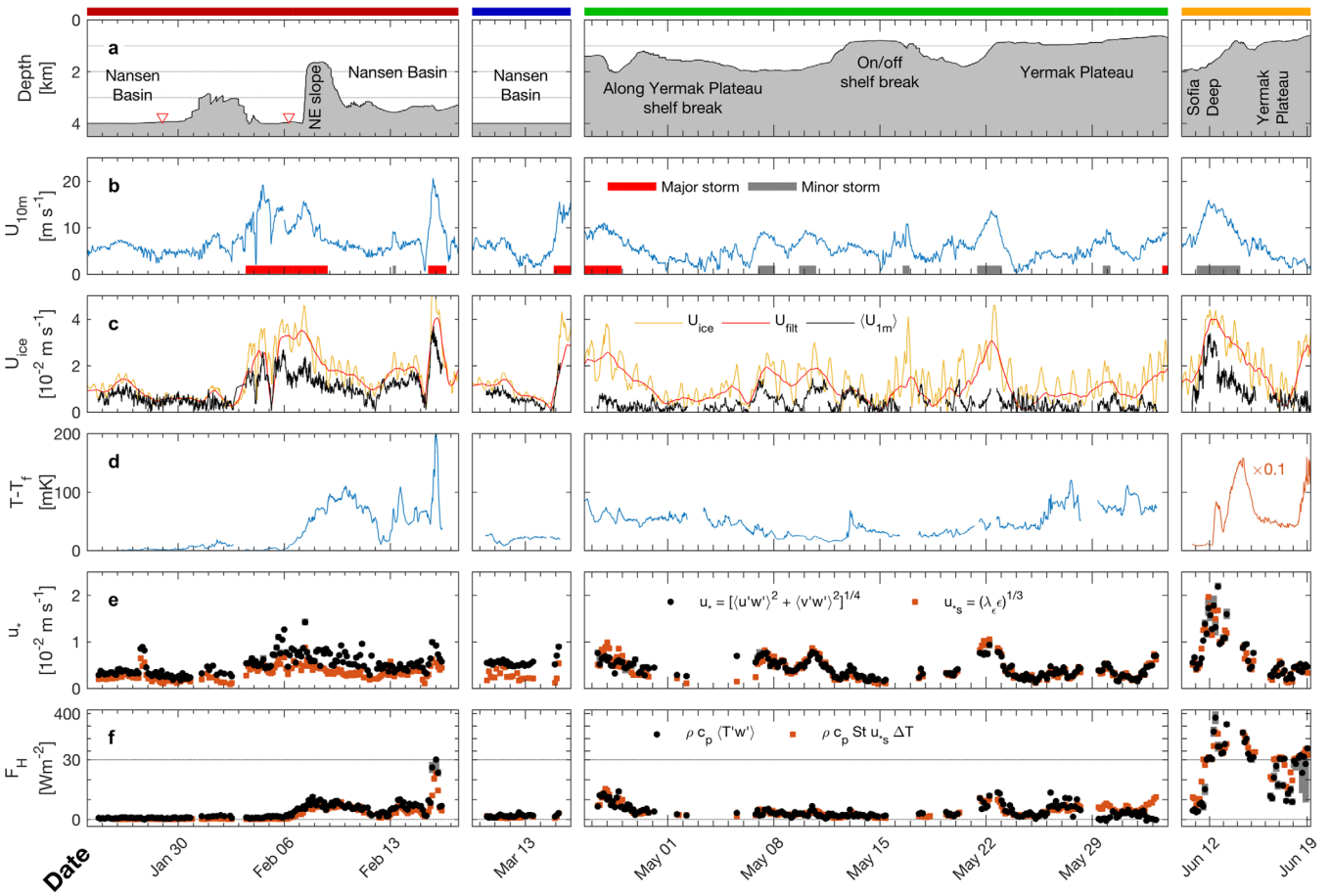

Figure 3. Time series of (a) water depth (ETOPO-1), (b) 10 m wind speed, with storms indicated by horizontal bars, (c) filtered (demodulated using diurnal and semidiurnal periods) and unfiltered ice drift speed and current magnitude at 1 m (black), (d) temperature above freezing (note factor of 10 reduction in fourth panel), and 3 hourly averaged values of (e) friction speed from covariance measurements (u_*, black) and vertical velocity spectra (u_{*s}, red) and (f) heat flux for the four TIC deployments. Parameterized heat flux is shown in red. Note the change in vertical scale above 30 W m^{-2} in Figure 3f. Error bars for friction velocity and heat flux indicate 95% confidence limits from bootstrap calculations.

Floe 2 drift was confined to the Nansen basin, at depths greater than 3900 m. The under-ice turbulence record from Floe 2 covers about 6 days. A passing storm between 14 and 16 March broke up the ice floe, disconnected the power cord, and thus terminated the record on the night of 15 March. Ice drift speeds were on average 30 cm s^{-1} during the storm, compared to 10 cm s^{-1} the week prior.

Floe 3 drifted over the eastern flank and top of the YP. Depths during TIC deployment varied between 600 and 2000 m. Our measurements here started during a major storm event, and throughout May, several minor storms were encountered. The wind speed averaged over the duration of the storms was 9.3 m s^{-1}, compared to 4.6 m s^{-1} otherwise. Over the plateau, the ice drift speed was affected by tides as well as wind (Figure 2b), and diurnal variation in drift speed can clearly be seen from Floe 3 (Figure 3c). Mean ice speed during the storms was 25 cm s^{-1}, whereas excluding storms gives a mean of 11 cm s^{-1}. Onset of ice bottom melt was observed on 31 May by hot-wires [*Rösel et al.*, 2016], concurrent with the ice camp drifting over warmer AW.

Floe 4 was a drift during rapid melting conditions [*Itkin et al.*, 2015]. Ice bottom melt started on 12 June. The first melt pond was observed on 9 June, and the onset of snow melt was recorded on 14 June (A. Rösel, personal communication, 2016). The drift covered from the Sofia Deep to up the slope of the YP. A storm passed between 11 and 14 June, with a peak wind speed of 17.3 m s^{-1} and drift speed up to 44 cm s^{-1}.

An overview of the hydrographic and ocean current conditions during the experiment is given by A. *Meyer et al.* [2017]. AW or modified-AW is present in the water column for the whole drift, although warmer and shallower close to the Svalbard continental slope, where the main branch of the West Spitsbergen current

flows along the topography [*Meyer et al.*, 2017a]. Over the deep basin, tidal forcing is weak, whereas over the shelf slope both the M2 and K1 tidal constituents become significant (Figure 2b) [see also *Padman et al.*, 1992; *Fer et al.*, 2015].

3. Measurements in the Under-Ice Boundary Layer

3.1. Turbulence Instrument Cluster

Turbulence instrument clusters (TICs) were deployed through a hole in the ice to measure turbulent fluxes in the ice-ocean boundary layer. The hydrohole was located a few hundred meters away from the ship to avoid sampling in its wake, and was covered with styrofoam to avoid refreezing. Each cluster acquires sufficiently high-frequency measurements of ocean currents, temperature, and conductivity to resolve the turbulent momentum and heat fluxes, together with the salinity, all at approximately the same measurement volume. A set of two TICs were deployed, located at approximately 1 and 5 m below the ice undersurface. The TIC at 5 m failed to return good quality data in 90% of the total duration of the experiment. We therefore concentrate on the continuous time series obtained from the cluster 1 m below the ice.

Currents were measured by a Sontek acoustic Doppler velocimeter (ADV), sampling a 2 cm^3 volume 18 cm from the transmitter at 24 Hz, averaged to 2 Hz temporal resolution. Temperature and conductivity were measured using Sea-Bird Electronics sensors (SBE3F and SBE4, respectively), sampling at 24 Hz, averaged to 3 Hz. Additionally, the TIC was equipped with a microconductivity sensor (SBE7) on Floes 2–4.

Two slightly different setups were used during the field campaign. On Floe 1, the TICs were mounted on a fixed pole, requiring manual rotation to align with the mean flow, a setup previously used by *Randelhoff et al.* [2014]. Upon retrieval, the mast and the instrumentation were severely damaged and could not be used for the remainder of the campaign. From Floe 2 onward, another TIC mast, equipped with similar but not identical sensors, was suspended on a wire and equipped with a vane, freely rotating to face the current. This general setup and instrumentation is identical to that of *McPhee et al.* [2008] and *Sirevaag* [2009]. A pressure sensor is used to infer the exact depth of the sensors until mid-May when the pressure sensor failed. For the remaining period, the depth of the clusters was estimated manually. At times of rapid melt, the instrument depth was controlled daily.

3.2. Covariances, Friction Velocity, and Heat Flux

The processing of data from TICs follows standard methods reported thoroughly in earlier studies [*McPhee*, 2002, 2008]. The time series is split into 15 min segments. The motivation for the choice of the segment length is discussed in section A4. For each segment, currents are aligned with the mean current, so that cross stream and vertical current components average to zero, $\langle v\rangle=\langle w\rangle=0$. Time averages are indicated by angled brackets, $\langle\cdot\rangle$. Temperature (T), salinity (S), and current components (u, v, and w) are then detrended to obtain the fluctuating ($\cdot'$) parts.

Covariances $\langle u'w'\rangle$, $\langle v'w'\rangle$, and $\langle T'w'\rangle$ are calculated to obtain the Reynolds stress components and the kinematic vertical heat flux, respectively. Confidence intervals for the covariance calculations are obtained using the bootstrap method following *McPhee* [2008, pp. 46–51]. Each 15 min time series is resampled 1000 times to make an estimate of the likelihood of our sample mean happening by chance. Covariance estimates are averaged in bins of $n = 12$ (3 h), and assuming the individual covariances are normally distributed, the 95% confidence intervals for the true mean can be calculated as [*McPhee*, 2008]

$$CI_n=\bar{X}_n\pm1.96\sigma_n/\sqrt{n}, \tag{1}$$

where $\bar{X}_n$ is the mean of n covariance calculations and σ_n is the mean bootstrap standard deviation. Friction velocity is calculated from

$$u_*=\left[\langle u'w'\rangle^2+\langle v'w'\rangle^2\right]^{1/4}, \tag{2}$$

together with the 95% confidence limits from the bootstrap calculations. Turbulent heat flux in units of W m^{-2}, is obtained from

$$F_H = \rho_w c_p \langle T'w' \rangle, \tag{3}$$

where ρ_w is the water density and c_p is the specific heat of seawater.

The data set is acquired under highly variable environmental forcing conditions, and is therefore subjected to an extensive quality control, fully described in Appendix A. After ensuring basic data quality for the SBE temperature and salinity sensors (section A1), noise levels of the current measurements are obtained (section A2), and a set of objective criteria are applied to each 15 min segment in order to identify and exclude questionable data affected by noise and swell, or defy the assumption of stationarity and Taylor's frozen turbulence hypothesis (section A3).

Based on our quality control, 19% of 6014 data segments are excluded from further analysis. The majority of the rejected data was from winter, caused by the lack of scatterers in the water. In total, approximately 50 days of high-quality turbulence data are retained.

3.3. Heat Flux Parameterization

A parameterization of the oceanic heat flux from bulk properties is desirable, given the inherent difficulties of direct measurements. The oceanic heat flux depends strongly on the interface friction velocity, u_{*0}, and temperature elevation above freezing. From observations of heat flux and Reynolds stress during MIZEX, *McPhee* [1992] suggested a simple bulk parameterization of heat flux,

$$F_{H,bulk} = \rho_w c_p \mathrm{St} u_{*0} \Delta T, \tag{4}$$

where $\Delta T = (T - T_f)$ is the mixed-layer temperature elevation above its freezing temperature and St is the turbulent Stanton number. In practice, we use temperature and salinity measurements from the TIC at 1 m below the ice. From the yearlong SHEBA drift, an average value of $\mathrm{St} = 0.0057 \pm 0.0004$ was found, with no apparent dependence on Reynolds number (we refer to this as the canonical value of St) [*McPhee*, 2008, pp. 116–118]. Friction velocity from covariances measured by the TIC 1 m below ice (u_*, equation (2)) can be used here, but we opt for a less noisy alternative and use u_{*s} calculated from the spectra of vertical velocity (section 3.4).

3.4. Mixing Length and Dissipation Rate

Mixing length is the vertical distance over which energy-containing turbulent eddies effectively diffuse momentum. The mixing length, λ_M, can be estimated from the inverse of the wave number at the peak in the variance-preserving form of the vertical velocity spectrum [*McPhee*, 1994]. In practice, we calculate the wave number, k, spectrum of vertical velocity, $\Phi_w(k)$, for each 15 min segment, obtain the weighted spectrum as $k\Phi_w$, logarithmically bin in k, fit a tenth order polynomial, and then detect its maximum value and the corresponding wave number k_{max}. Mixing length is then obtained as $\lambda_M = 0.85/k_{\mathrm{max}}$, where k_{max} is in radian units.

In the inertial subrange of $\Phi_w(k)$, the dissipation rate of turbulent kinetic energy, ε, depends only on the local wave number and the spectral density through

$$\Phi_w(k) = \frac{4\alpha_\varepsilon}{3} \varepsilon^{2/3} k^{-5/3}, \tag{5}$$

where the constant $\alpha_\varepsilon = 0.51$ has been determined from laboratory and atmospheric experiments [*McPhee*, 2008, p. 57]. We obtain ε from a (k, Φ_w) value read from the inertial subrange, identified by the $-2/3$ slope in $k\Phi_w$ (or the $-5/3$ slope in Φ_w).

From mixing length and dissipation rate we calculate an independent, spectrally-derived friction velocity [*McPhee*, 1994],

$$u_{*s} = (\varepsilon \lambda_M)^{1/3}. \tag{6}$$

This method, using the vertical component of the velocity measurement, results in less noisy u_{*s} in low signal-to-noise ratios for two reasons: (i) w spectra are relatively less noisy than the horizontal component as a result of transducer configuration (see Appendix A) and (ii) the detection of a well-defined inertial subrange required for equation (5) excludes any spectrum with a small dynamical range. The noise level of u_* is discussed in section A2.

The mixing length is an uncertain parameter, both because of the spectral wave number bandwidth and the assumptions inherent in the method. Uncertainty propagated to the friction velocity u_{*s}, however, is small: for an assumed 50% error in ε and λ_M, assuming independent random error, the resulting uncertainty in u_{*s} is approximately 24%.

4. Results

Over the course of the four deployments we observe a wide range of heat fluxes (Figure 3f), from typically near-zero upward fluxes in winter and interior basin to several hundred W m^{-2} over the plateau when ice melt is reinforced by wind forcing and warmer underlying waters. Friction velocity (Figure 3e) generally responds to variations in wind forcing and the mobility of the ice pack. In the following, we present a floe-by-floe overview of the heat flux and friction velocity statistics based on 15 min values. Temperature is given as the elevation above the salinity-determined freezing point, $\Delta T = T - T_f(S)$, in units of milli Kelvin (mK).

On Floe 1, average vertical heat flux is 3.8 W m^{-2}. Prior to 6 February, wind is relatively calm and drift is slow over the abyssal plain. Temperature is near freezing ($\langle \Delta T \rangle = 2.9$ mK) and heat fluxes are small ($\langle F_H \rangle = 0.9$ W m^{-2}). The storm on 3 February accelerates the ice, and from 6 February temperatures rise to $\Delta T = 110$ mK accompanied with an increase in turbulent heat flux. Between 6 and 12 February, $\langle F_H \rangle = 6.1$ W m^{-2}, with a maximum of 11.3 W m^{-2}. The elevated heat fluxes correspond to the drift over shallower topography on the eastern slope of the YP where the mixed-layer temperature is higher. Water temperature approaches freezing again on 12 February, but rises in response to the passage of an intense storm, peaking at $\Delta T = 240$ mK on 16 February. Heat fluxes increase to $F_H = 31$ W m^{-2}, and $\langle F_H \rangle = 7.4$ W m^{-2} between 12 and 17 February. Friction velocity averages to 4 mm s^{-1} prior to 6 February, and 6 mm s^{-1} after. Note that the velocities for Floe 1 have been filtered to remove the contamination by noise (see section A1), and friction velocity is likely underestimated.

The entire Floe 2 drift is over the deep Nansen basin. Temperature is slightly higher than during the first part of Floe 1 ($\langle \Delta T \rangle = 21$ mK), and heat fluxes are nearly doubled ($\langle F_H \rangle = 1.7$ W m^{-2}). This is consistent with differences seen in the upper mixed layer between Floe 1 and Floe 2 [*Meyer et al.*, 2017]. Using idealized one-dimensional modeling, I. Fer *et al.* [2017] attribute this mainly to entrainment of warm water from below. On 14 March, a storm accelerated the ice drift, but the ice broke up, and the instruments lost power before the storm peaked. The highest heat flux observed on Floe 2 was 3.2 W m^{-2}, but does not include possibly larger values during the storm.

The drift of Floe 3 is the longest, moving along the slope of the YP (depths less than 2000 m), before drifting over the plateau after 22 May. Available heat at the sensor depth ($\langle \Delta T \rangle = 46$ mK) is about twice that of Floe 2, and heat flux averages to $\langle F_H \rangle = 3.8$ W m^{-2}. During the five storms, heat fluxes average to 6.3 W m^{-2}, a doubling compared to periods without storms ($\langle F_H \rangle = 3.1$ W m^{-2}).

Floe 4 covers a period of rapid melt, when ocean-ice heat fluxes are enhanced by the passage of a storm. Temperature is 91 mK above freezing the day before the storm, and increases to 840 and 1600 mK in two separate peaks; 1 day after the peak wind forcing, and then by the end of the storm. The first peak is associated with stronger wind forcing and higher drift speed. Turbulent heat fluxes averaged over a 12 h window centered at each temperature peak are $\langle F_H \rangle = 286$ W m^{-2} and $\langle F_H \rangle = 140$ W m^{-2}, respectively. The maximum heat flux was observed with the first peak, reaching 578 W m^{-2} (3 h average, 367 W m^{-2}). There is an 18 h data gap in observations during the storm. Excluding the storm and the following first day from the calculations, the heat fluxes are still relatively high compared to other drifts, $\langle F_H \rangle = 46$ W m^{-2}. Averaged over all of Floe 4, $\langle F_H \rangle = 63$ W m^{-2}, reflecting the frequent moderate heat fluxes. Also, occasional negative values are observed, notably in the two final days of the drift, and tend to lower the 3 h averages which remain positive throughout. Friction velocity is 11 mm s^{-1} on average, and reaches a maximum of 22 mm s^{-1}, which is also the largest throughout the campaign.

Estimated mixing length is highly variable on short timescales, leading to large error bars on daily averages (Figure 4b), but the campaign average value ($\pm$one standard deviation) is $\lambda_M = 0.54 \pm 0.20$. The mode value (0.44) is close to the mixing length for neutral stratification, $\kappa z = 0.4$, expected at a distance $z = 1$ m from the boundary in the constant stress boundary layer using von Kármán's constant $\kappa = 0.4$. Dissipation rates of

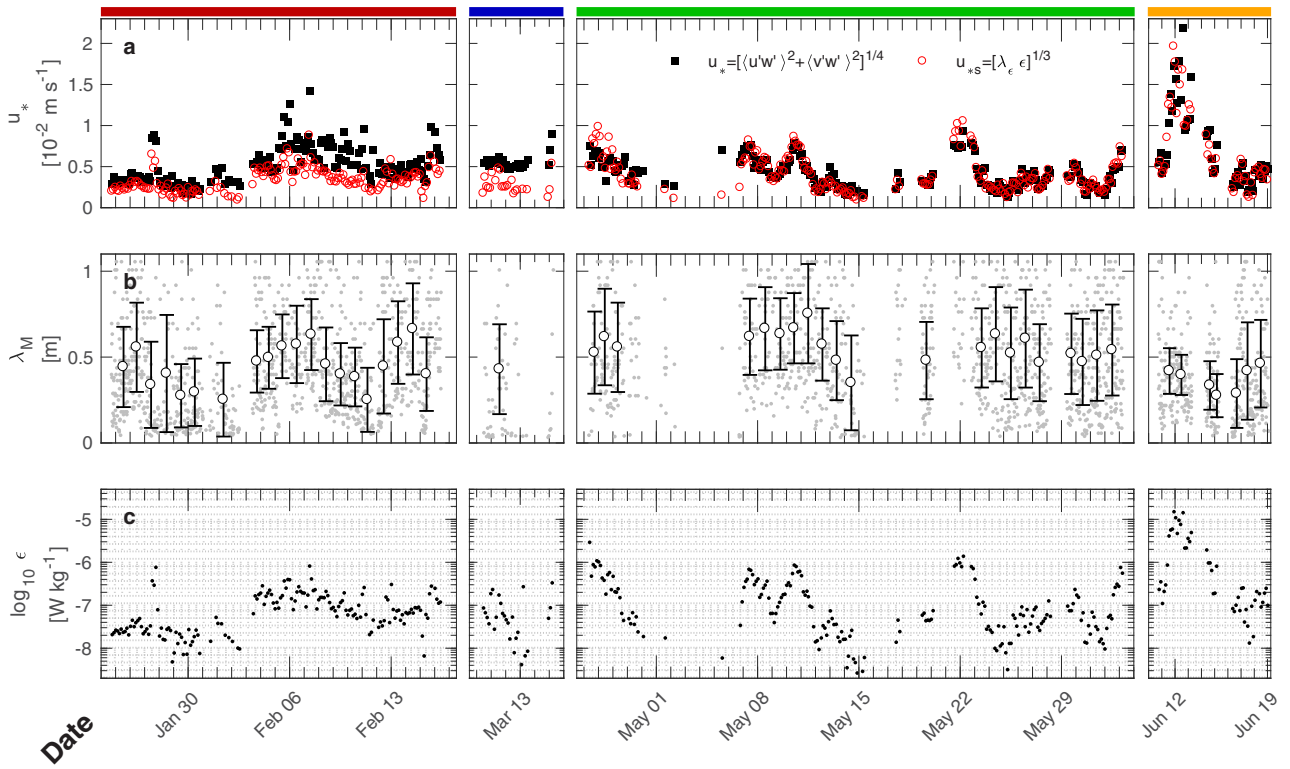

Figure 4. Time series of variables derived from spectra of vertical velocity. (a) Friction velocity from covariance (black) and from spectra of vertical velocity (red). (b) Mixing length (dots), daily average (circles) and one standard deviation envelope. (c) Dissipation rate of turbulent kinetic energy, ε, calculated as described in section 3.4.

turbulent kinetic energy span 4 orders of magnitude, from $\varepsilon \sim 10^{-9}$ W kg^{-1} in quiescent periods of Floes 1–3, to a maximum of $\sim 10^{-5}$ W kg^{-1} during the wind event in Floe 4.

5. Discussion

Momentum transfer from atmosphere to ocean drives mixing of the upper ocean. Typically the observed ocean heat flux to sea ice is a combination of several factors, including solar heating of the upper layer, salt and heat fluxes from sea ice melt, and the vertical mixing of heat from underlying warm water by wind from above or by tides over topography. Differences are large between the deep basin and over the continental slope where AW resides. We attempt to separate and quantify these factors.

5.1. Wind-Forced Mixing

The absence of solar heating in winter allows us to estimate the contribution of oceanic heat from below to observed heat fluxes during Floes 1 and 2. Floe 1 drifted in complete darkness, and during Floe 2 solar angles were low enough that we can assume no solar heating under the ice. The two floes were mostly confined to the deep basin, away from significant tidal mixing (Figure 2). We thus consider the observed heat fluxes to be wind forced, and representative of deep basins in the Arctic Ocean. Over the deep basin ($D > 3750$ m), $\langle F_H \rangle = 1.4 \pm 1.6$ W m^{-2} ($\pm$ one standard deviation) from January through March. The median value is 0.9 W m^{-2} and is representative of the quiescent periods. Calculated over storm periods, the average heat flux in winter is 2.1 ± 2.3 W m^{-2}, while for quiescent periods the average is 1.0 ± 1.1 W m^{-2}. The comparatively high standard deviations reflect the high temporal variability and the importance of individual events. The occurrence distribution of the observed heat fluxes is shown in Figure 5, and it is clear that storm events in winter shift the distribution toward higher, although still modest, heat fluxes. Using a simple one-dimensional model, *Fer et al.* [2017] show that the hydrographic evolution of the upper ocean during the N-ICE2015 winter drift can be fairly well reproduced from realistic forcing from variable profiles of eddy diffusivity in the water column. The increase in heat flux during winter storms can be attributed to entrainment of relatively warm waters from deeper in the water column.

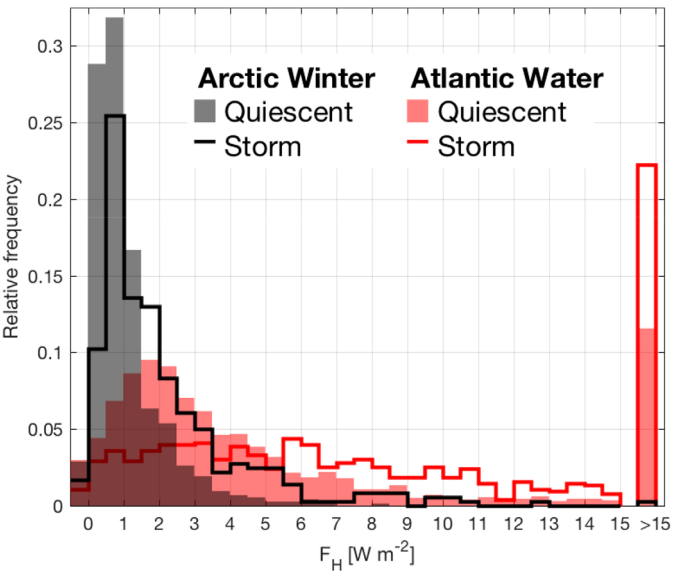

Figure 5. Histograms showing relative frequency of occurrence of ocean-to-ice heat flux during Arctic winter (black, identified as depths $D > 3750$ m) and over Atlantic Water influence (red, $D < 2000$ m). Data from storm periods (lines) show a shift toward higher heat fluxes compared to quiescent (shading) in both cases. 21 and 10% of the fluxes over Atlantic water are >15 W m^{-2} during storms and quiescent conditions, respectively, and are bulked together in the rightmost column.

Relying on the bulk parameterization applied to data from drifting buoys, *McPhee et al.* [2003] estimated an annual average heat flux of 2.6 W m^{-2} over the deep Arctic Ocean, by assuming zero heat flux from January through April. This suggests that the winter values can account for approximately one third of the annual average heat flux in the central Arctic. Using eddy covariance measurements at 6 m on ice-tethered profilers in the Canada Basin, *Cole et al.* [2014] found October–April average heat flux of 1.0 ± 2.9 W m^{-2}, comparable to our observations.

One event worth highlighting is from the storm in early February. The storm causes the ice camp to retroflect and cross its own track (Figures 1 and 6a). The times of passages at the intersection (I1 and I2) are approximately 1 week apart (red triangles in Figure 3a), and can give some insight into the temporal variability. Figure 7 contrasts 1 week time series of selected parameters surrounding I1 and I2, and Table 2 lists their mean values over 24 h, centered at the intersection. The first passing, I1, is during calm conditions, slow ice drift, and near-zero heat flux. The second passing, I2, is during strong winds and high drift speed, where temperature at the measurement depth is higher and the observed heat flux is four times larger than during I1. The rapid turning of the wind (Figure 7a)

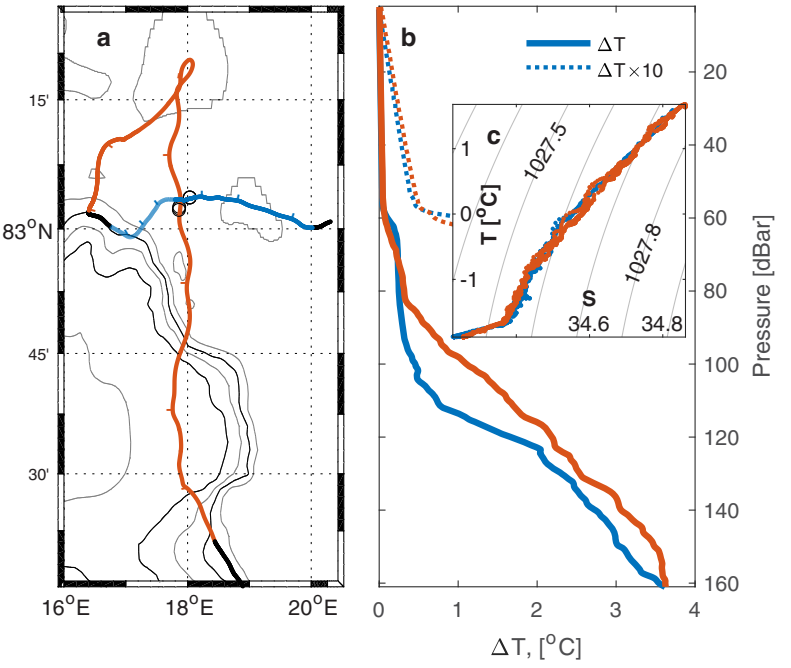

Figure 6. (a) Map of the drift trajectory around the intersection. One week surrounding the I1 (blue) and I2 (red) intersects correspond to the time series in Figure 7. (b) Average profiles of temperature above freezing from three MSS casts nearest the crossing I1 (blue) and after I2 (red) (see Figure 7), marked by circles in Figure 7a; corresponding temperature-salinity diagram is shown in Figure 7c.

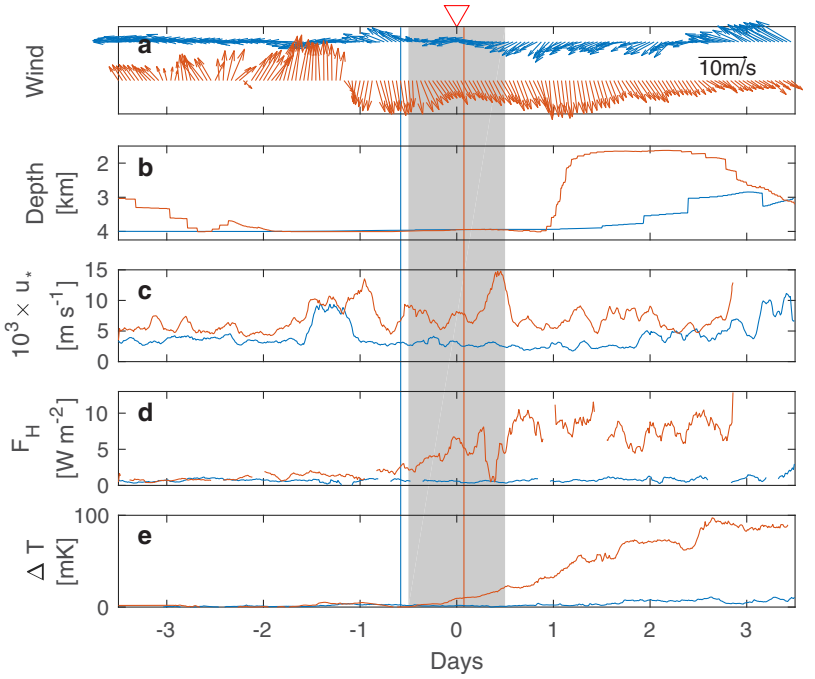

Figure 7. One week time series of (a) wind, (b) depth, (c) friction speed, (d) heat flux, and (e) temperature above freezing, centered on each of the two crossings I1 (blue) and I2 (red) (see Figure 6). Gray patch envelopes the 24 h window used to calculate average values in Table 2, and the times of profiles used in Figure 6 are indicated by vertical lines. Here wind arrows are 1 h running average, 15 min values are used for u_* and F_H.

accelerates the ice pack southward, breaking up the ice. At this time, strong shear and divergence of the ice cover is observed as the sea ice concentration dips below 100% (P. Itkin *et al*., Thin ice and storms: Sea ice deformation from buoy arrays deployed during N-ICE2015, submitted to *Journal of Geophysical Research*, 2017). Profiles of temperature (Figure 6b) and salinity reveal a rise in the pycnocline of approximately 10 m, and there is an increase in mixed-layer (top 58 m) temperature above freezing of 4.5 mK. The similar TS properties (Figure 6c) indicate that the water mass is essentially the same, and the change in the profiles is likely due to local processes, rather than, e.g., a shift in the AW layer. This is supported by the findings of *Fer et al*. [2017]. The divergence of the ice field in response to northerly winds could also drive upwelling of the pycnocline, as was previously observed by *McPhee et al*. [2005].

While the first half of the experiment drifts over the deep basin, Floes 3 and 4 are typically located over the slopes or the Yermak Plateau. The main pathway of AW north of Svalbard crosses the saddle of the YP, and continues along the continental shelf slope, while another branch follows the slope around the north side of YP, before reconnecting with the main branch [*Rudels et al*., 2000; A. Meyer *et al*., 2017a]. Elevated oceanic heat fluxes in proximity to AW were reported by *Sirevaag and Fer* [2009], who observed surface heat fluxes of order 100 W m^{-2} over the branches of the West Spitsbergen current. From a buoy drift over the YP, *McPhee et al*. [2003] found that basal heat flux was dominated by mixing of the underlying warm water over the plateau, reaching up to 100 W m^{-2}. We therefore expect elevated heat fluxes here compared to the deep basin, and the circulation pattern is in part reflected in the observed heat fluxes (Figure 8). The southernmost track (Floe 4) passes over the main pathway of AW, where we observed the highest heat fluxes. Also, observations made between the eastern flank of YP and the continental slope (Floe 1) show elevated heat fluxes relative to other locations; however, these occurred under severe wind forcing. Away from these branches and the shelves, heat fluxes were typical of the central Arctic.

Table 2. Average Wind Speed (U_{10}), Friction Velocity (u_*), Heat Flux (F_H), Temperature Above Freezing (ΔT), and Ice Speed (u_{ice}) Over 24 h Centered on the Two Intersection Passings I1 and I2, Indicated by Gray Shading in Figure 7

	I1	I2
U_{10} (m s^{-1})	4.5	12.8
u_* (10^{-3} m s^{-1})	3.0	8.2
F_H (W m^{-2})	0.54	2.3
ΔT (mK)	1.3	7.1
u_{ice} (cm s^{-1})	5.5	34

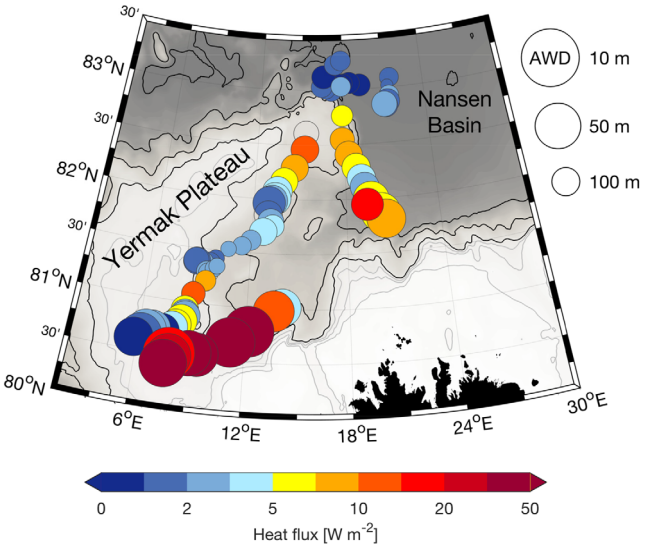

Figure 8. Map of daily averaged observed upward ocean-ice heat flux along the drift track (colors). Circle size scales inversely with the depth of the Atlantic Water layer (AWD, inferred as the depth of the 0°C isotherm).

The relative influence of topographic features and the presence of AW on the observed heat fluxes cannot be separated using the present data set. Because the boundary current carrying the AW follows the bathymetry, the drift over the AW branches is always colocated with rough topography. For depths $D < 2000$ m, AW or modified-AW is typically present, and the histogram of heat flux (Figure 5) is markedly different from the Arctic Winter case. The mode value is approximately twice as large ($\sim$2 W m^{-2}), median is four times greater (3.6 W m^{-2}), and the mean value over all data where $D < 2000$ m is $\langle F_H \rangle = 15.5 \pm 54\,\mathrm{W\,m^{-2}}$, reflecting how episodic occurrences of heat fluxes greater than 15 W m^{-2} (7%, Figure 5) dominate the mean and variability. When subsampled over quiescent periods with $D < 2000$ m, $\langle F_H \rangle = 10.8 \pm 42.3\,\mathrm{W\,m^{-2}}$. During storms, the average heat flux increases to $\langle F_H \rangle = 27.8 \pm 76.4\,\mathrm{W\,m^{-2}}$.

Toward the end of Floe 3, incident solar radiation becomes significant, as evident from the encounter of an under-ice phytoplankton spring bloom on 25 May [*Assmy et al.*, 2017]. Effects of solar heating and sea ice melt dominate observations from the remainder of the campaign.

5.2. Solar Heating and Sea Ice Melt

Solar radiation is a major source of heating in the surface mixed layer [*Maykut and McPhee*, 1995; *McPhee et al.*, 2003; *Shaw et al.*, 2009; *Gallaher et al.*, 2016]. In summer, solar radiation heats the upper ocean through openings in the ice cover and through melt ponds, which then can reach the ice from below. Floe 4 drifts onto the YP in June, and snowmelt, melt ponds, and rapid ice bottom melt were observed concurrently with the highest heat fluxes throughout the campaign.

The presence of AW north of Svalbard is the cause of the typically low sea-ice extent in the area [*Rudels et al.*, 2004; *Onarheim et al.*, 2014], and the AW constantly loses heat to the surface water, melting or preventing the formation of sea ice. While AW flows near the surface during the whole Floe 4 drift (Figure 8) (see also A. Meyer *et al.*, 2017a), the floe drifts near the ice edge (Figure 1), and the wind event between 11 and 14 June takes the ice over waters which were recently exposed to solar radiation. The observed heat fluxes in the later part of the experiment (Floe 4) are thus caused by a combination of heat from the AW layer from below and solar heating of the upper ocean [*Taskjelle et al.*, 2016], as well as effects of freshwater from the melting ice.

The low sea ice concentration and proximity to the ice edge (P. Itkin *et al.*, submitted manuscript, 2017) enhance solar heating of the upper mixed layer, and can at least in part account for the large heat fluxes observed in Floe 4. During its last days, Floe 3 drifted parallel to Floe 4, but observed heat fluxes here were 1–2 orders of magnitude lower, which can be related to the greater distance from the ice edge. The ice edge from 17 June shown in Figure 1 is representative of June ice extent. The mean distance between these two drift segments was 30 $\pm$ 5 km ($\pm$one standard deviation, distance is taken as that to the nearest point on the Floe 4 track from the position Floe 3 at each time). Similar observations were made by *Morison et al.* [1987] and *McPhee et al.* [1987] during the Marginal Ice Zone Experiment (MIZEX) in June 1984. The final days of Floes 3 and 4 are colocated with the ice station drift of the Polar Queen in 1984. In the same season, they drifted near the ice edge, and across a temperature front which corresponded to the recent position of the ice edge. They found that periods where the ice floe drifted over recently ice-free waters, additionally warmed by insolation, dominated the heat budgets.

During parts of the drift, heat fluxes measured at the TIC are occasionally reduced relative to what would be expected from a standard bulk parameterization (see section 5.3). Two possible explanations exist: solar heating, which can invert or weaken the temperature gradient, or near-surface intrusions of meltwater which skews the ice-ocean interface heat balance. Both explanations are explored below.

Differential heating increases with the observed spring bloom (P. Assmy *et al*., submitted manuscript, 2017), as a greater fraction of the light is absorbed in the top layer [*Taskjelle et al*., 2016]. While this typically stabilizes the surface layer, turbulent mixing would lead to a downward flux of this heat. As the ice floe drifts from warmer to cooler waters, shear drags warm water near the boundary over cooler water below, setting up a positive vertical temperature gradient. The warm water lens may be located above the sampling volume, which may explain why observed vertical heat fluxes at 1 m are significantly reduced, or even negative, while the true heat flux to the ice undersurface is still strongly positive in later parts of Floe 4. Indeed, while heat flux measured by the TIC for example on 14 June is equivalent to about 4 cm of melt, nearby ice thickness measurements from hot wires show a 24 cm reduction in ice thickness [*Rösel et al*., 2016]. The same mechanism was proposed to explain the negative heat fluxes observed by *McPhee* [1992], and for significantly reduced heat fluxes observed by *Sirevaag* [2009] as they drifted over a horizontal temperature gradient. When this mechanism dominates, it is likely that the true oceanic heat flux to the ice is significantly greater than observed at the 1 m measurement level.

The second possibility to explain apparent reductions in heat fluxes measured at 1 m below the ice-ocean interface is that the melting ice can also introduce lateral freshwater fluxes. Parameterized heat flux follows the observed values throughout the experiment (see section 5.3), except for two periods in the last days of Floe 3. Two wind events passed the ice camp between 29 May 17:00 and 30 May 05:00, and between 2 and 6 June (peak wind speeds 10.6 and 13.7 m s^{-1}, respectively, Figure 3b). Friction velocity was higher during the two storms ($\langle u_* \rangle = 5.7$ mm s^{-1}) compared to the calm period between the storms ($\langle u_* \rangle = 2.9$ mm s^{-1}). These dates match with periods when $F_{H,\mathrm{bulk}}$ underestimated F_H (Figures 9a and 9b). Using a similar set of observations of ice-ocean heat fluxes in late summer, *Randelhoff et al*. [2014] observed that the bulk heat flux formula (equation (4)) frequently overestimated the measured heat flux. As an explanation, they suggested that atmospheric (non-oceanic-derived) ice melt could create additional freshwater at the ice-ocean interface which increases the ice-ocean interface freezing temperature, thereby effectively skewing the balance between

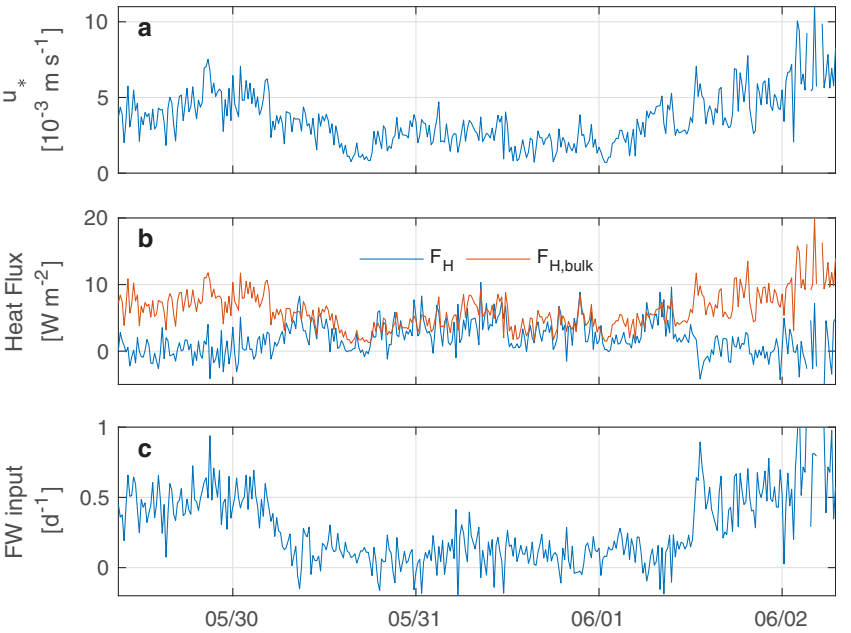

Figure 9. Time series from the period where parameterized heat flux deviates significantly from measured heat flux, showing (a) friction speed, (b) observed and parameterized heat flux, and (c) calculated equivalent freshwater input.

oceanic heat and salt fluxes and reducing the ice-ocean temperature gradient [*Randelhoff et al.*, 2014, equation (14)].

Following the equations given by *Randelhoff et al.* [2014], we estimate the additional (from non-oceanic melt) salt flux that would be necessary in order to achieve this reduction in heat flux within the three-equation formalism [*McPhee*, 2008]. With the ratio of heat to salt transfer coefficients of R = 70 [*Notz et al.*, 2003] and assuming conductive heat flux through the ice $q_c = 0$ (summer conditions), ice bulk salinity $S_i = 5$ and interface salinity $S_0 = 30$, this results in an "additional" salt flux of approximately 0.5 m d^{-1} during those periods, or meltwater entrainment equivalent to 2 cm d^{-1} of ice melt (Figure 9c). Basal melt rates at that time estimated from ice mass balance data [*Itkin et al.*, 2015] were O(1 cm d^{-1}), hence, it is possible that the equivalent of 2 cm d^{-1} was diverted into leads over several preceding days. Lateral melting of ice floes, aided by water warmed in leads, might have contributed, but if the "additional" salt flux term were to explain the entire discrepancy, a buildup of the additional freshwater pool (from either leads or percolation) on the order of a few days would be required.

We conclude that the deviation from the bulk Stanton-number formula at the end of Floe 3, or at least part of it, can be explained using the more general form of *Randelhoff et al.* [2014] if during the wind events, meltwater previously accumulated in leads was entrained into the ice-ocean molecular sublayer approximately at a rate of 2 cm d^{-1}. Counter-intuitively, wind events during the melting season might therefore (temporarily) have reduced ocean cooling by inserting a disproportionately low-salinity (thus "high"-temperature) layer between oceanic heat and the melting ice. This explanation is also consistent with visually observed accumulation of freshwater in instrument holes during strong melting conditions (A. Meyer, personal communication, 2016). In addition, the ice cover was weakly convergent during that time (P. Itkin *et al.*, submitted manuscript, 2017), indicating that meltwater may have been pushed out of the leads, contributing to entrainment of freshwater into the ice-ocean boundary layer.

5.3. Parameterized Heat Flux

Agreement between the heat flux measured by covariance and the one estimated by the bulk parameterization (equation (4)) using the canonical value of the Stanton number was typically good, with a correlation of r = 0.82, reflecting the variability in wind forcing (u_*) and mixed-layer heat content (ΔT). A variable value for the bulk heat transfer coefficient (bulk Stanton number denoted by St_*) is calculated as the ratio between measured heat flux near the interface and the product of mixed-layer temperature above freezing and interface friction velocity,

$$St_* = \frac{\langle w'T' \rangle}{u_{*0}\Delta T}. \tag{7}$$

Different authors have noted a dependence of St_* on whether ice is melting or freezing at the bottom [e.g., *McPhee et al.*, 2008]. Freezing conditions are characterized by St_* on the order of 0.012 [*Cole et al.*, 2014], and the neutral and melting case is usually associated with the canonical value of about 0.0057. The ratio R, of heat and salt transfer coefficients is indicative of the strength of double-diffusive processes near the ice-water interface. Typical values of R during melting conditions are between 35 and 70 [*McPhee et al.*, 2008; *Notz et al.*, 2003], with a measured value of 33 north of Svalbard [*Sirevaag*, 2009], i.e., only melting conditions lead to substantial double-diffusive effects.

We group the data in three temperature categories: We define $\Delta T < 50$ mK as "near-freezing," 50 mK $< \Delta T < 200$ mK as "nonfreezing," and $\Delta T > 200$ mK as "warm." Observed and parameterized heat fluxes are grouped accordingly, and we find mean bulk Stanton numbers of $St_*(\text{near-freezing}) = 0.0108$ (0.0039, 0.0130), $St_*(\text{nonfreezing}) = 0.0061$ (0.0020, 0.0080), and $St_*(\text{warm}) = 0.0059$ (0.0024, 0.0072), where numbers in brackets indicate first and third quartiles.

Overall, our data set exhibits a tendency that the average bulk Stanton number (not accounting for a constant meltwater-induced offset) increases with lower values of ΔT, particularly below O(0.1 K) (Figure 10). We can conjecture that this indicates increasingly freezing-favorable conditions at low temperatures, and thus an overall gradual shift into the nondouble-diffusive freezing regime, characterized values of R near unity [*McPhee et al.*, 2008].

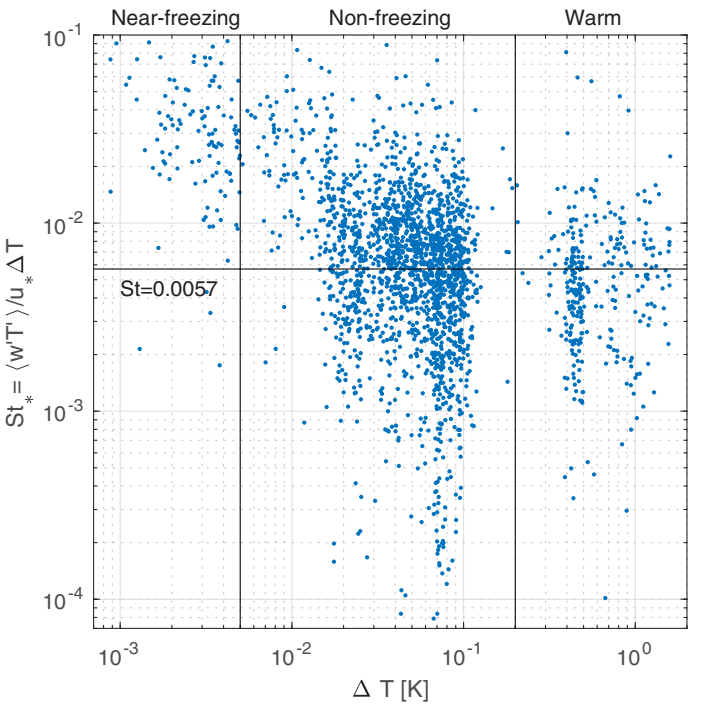

Figure 10. Temperature elevation above freezing versus bulk Stanton number. The three temperature groups (section 5.3) are indicated, separated by vertical lines. The canonical $St = 0.0057$ is shown for reference.

6. Conclusions

From direct measurements of under-ice turbulence in the Nansen Basin we find low, but nonzero upward heat fluxes in winter, averaging to 1.4 W m^{-2} with a standard deviation of 1.6 W m^{-2}, from January through March. Episodic events, such as a local upwelling event observed in February (section 5.1 and Figures 6 and 7), significantly increase heat fluxes and dominate variability. The proximity to Atlantic Water (AW) pathways and the shoaling of the AW layer are observed to increase the heat fluxes in winter by one order of magnitude (Figures 5 and 8).

Significantly higher oceanic heat fluxes are observed in spring. The observed heat fluxes are a combination of heat from the AW layer from below, solar heating at the surface, as well as effects of freshwater from the melting ice. Turbulent fluxes were particularly enhanced when the ice camps drift over topography near the YP or the northern slope of Spitsbergen. However, the presence of AW is not sufficient, and forcing is necessary to mix up heat toward the ice. We consistently observe enhanced mixing during wind events, and even more so when the ice is free to move. A wind event combined with drift over a shallow AW layer, resulted in 3 h average heat fluxes reaching 367 W m^{-2}, coinciding with rapid melt.

A commonly used bulk parameterization for heat flux is useful, and results in credible estimates in good agreement with observations. The bulk formula overestimates the heat flux on two occasions of increased wind forcing, both attributed to freshwater accumulated in leads, equivalent to approximately 2 cm d^{-1} of sea ice melt. Overall, while the parameterization successfully reproduces heat fluxes in winter conditions, more detailed process studies will be necessary to increase predictability of ice-ocean fluxes in conditions of rapid melt, solar heating, and strong lateral gradients.

Appendix A: Quality Screening

A1. Basic Quality Control

As a basic quality measure, temperature and salinity measurements from the two TICs at 1 and 5 m are compared for consistency. Temperature is concluded to be reliable for the whole deployment at both depths, while salinity at 5 m is discarded for Floes 1 and 3. Shorter periods with spurious salinity values are discarded from the 1 m sensor (e.g., salinity drift at start of a deployment). Furthermore, temperature and salinity are compared to measurements obtained from the microstructure sonde (MSS) [*Meyer et al.*, 2016], which was frequently used for profiling nearby. The MSS has itself been calibrated post-cruise against the ship's more accurate SBE CTD (A. Meyer *et al.*, Mixing rates and vertical heat fluxes north of Svalbard from Arctic winter to spring, submitted to *Journal of Geophysical Research*, 2017b). Using only data prior to 19 May, i.e., excluding the melting conditions, the mean difference between TIC and MSS measurements is 5 mK for temperature and 3×10^{-3} for salinity. There is no discernible difference in agreement with MSS between the two TIC-setups (Floe 1 versus Floes 2–3).

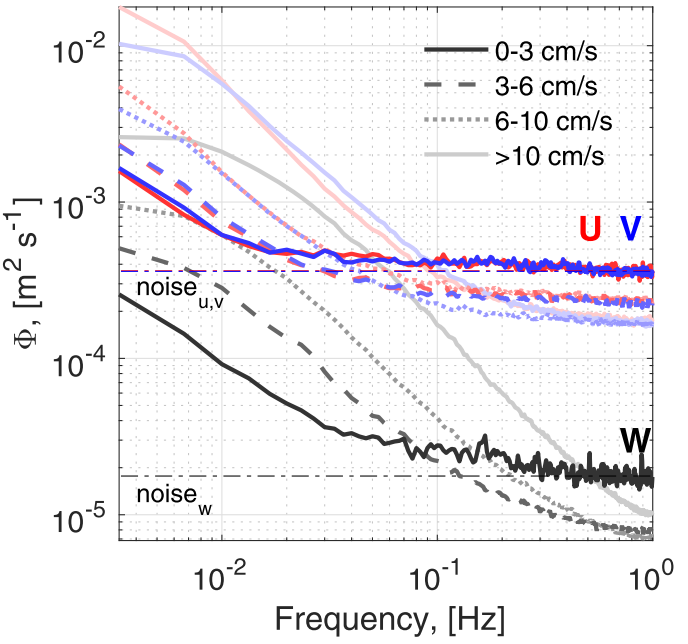

Figure 11. Frequency spectra of current velocity from the ADV, averaged in bins of mean current speed. Noise levels used in equation (A1) are indicated by horizontal lines.

A2. Noise Level

The SonTek ADVOcean user manual states a measurement accuracy for the ADV of ±1% or ±0.5 cm s^{-1}. The current meters depend on acoustic backscatter from particles suspended in the water. In the clear Arctic waters, particularly in winter, a lack of scatterers leads to low signal-to-noise ratios. We estimate the actual noise level of the current measurements from the velocity spectra, bin-averaged with respect to mean current speed (Figure 11). At high frequencies, white noise dominates over the signal, and we get an estimate of the noise level by integrating a white noise model spectrum (dotted lines in Figure 11) over the frequency domain,

$$\sigma_n = \int_0^1 \Phi_n df = \Phi_n|_0^1 \,, \qquad \text{(A1)}$$

$$\bar{u}_n = \sqrt{\sigma_n}. \qquad \text{(A2)}$$

Estimated noise levels for mean current speed <3 cm s^{-1} are $[u_n, v_n] \approx 2\times10^{-2}$ m s^{-1} and $w_n \approx 4\times10^{-3}$ m s^{-1}. The varying amount of scattering particles in the water does, however, call for a temporal varying noise estimate to be considered. From spectra of velocity for each 15 min segment, we only accept segments where average low-frequency (<0.02 Hz) spectral density is at least three times the average high-frequency (>0.1 Hz) levels. This ensures the dynamic range of the spectra, and the remaining segments are discarded as white noise.

The instrumentation and setup used in Floe 1 are identical to those used in *Randelhoff et al.* [2014] and suffer from similar noise issues. Following *Randelhoff et al.* [2014], we apply a first-order Butterworth low-pass filter with a cutoff frequency of 0.1 Hz to the Floe 1 current data. The cutoff frequency is chosen, based on spectral considerations, as the frequency where the white noise dominates, and is higher than that of *Randelhoff et al.* [2014] (0.0316 Hz). This fairly severe filtering lowers the fluxes uniformly, but the overall effect, not quantified here, depends on the turbulent length scale and mean advective velocity. While we preserve more of the variance relative to *Randelhoff et al.* [2014]'s filter, the resulting friction velocity and its variability are significantly reduced by this filtering. The effect of this on $\langle w'T' \rangle$ is a 9% average reduction, indicating that a small fraction of temperature-correlated variability is also removed.

We estimate the noise level of u_* from synthetic 15 min time series of u, v, and w, with variance equal to the noise obtained from spectra. The resulting u_{*n}=0.2 cm s^{-1} is an estimate of the covariance noise level for the experiment as a whole. Floe 2 data are from a low signal-to-noise ratio environment where we suspect covariances are dominated by noise (Floe 1 is filtered as described above). Noise level at Floe 2 is estimated visually as the lower range of observed values, $u_* \approx 0.5$ cm s^{-1}. The mean ratio u_*/u_{*s}=2.9 and 1.3, for Floe 2 and Floes 3–4, respectively. The larger discrepancy between u_* and u_{*s} on Floe 2 compared to Floes 3 and 4 indicate that the improvement using friction velocity from spectra over covariance is much larger in winter, when scatterer levels are low, compared to spring and summer.

A3. Systematic Quality Control

An objective set of criteria for automatic flagging of bad data is employed. Calculating covariances from point measurements require the Taylor's frozen field hypothesis to be satisfied, meaning that the turbulent structure can be considered "frozen" as it is advected past the measurement sensor

[*Thorpe*, 2007]. Each 15 min velocity time series segment is split into 1 min, half overlapping subsegments (29 data points), over which we calculate the mean and root-mean-squared quantities, further used in the following tests.

Taylor's hypothesis requires the flow to be stationary over the averaging period. To test for stationarity, we compare the 15 min time evolution of 1 min statistics (mean and root-mean-square, r.m.s.) to those calculated identically from synthetic Gaussian noise time series. If the cumulative time integral of the statistics is not significantly larger than that obtained from the noise, we deem that there is no trend or significant time variability in the statistics for the 15 min duration used in the covariance calculations, hence the stationarity assumption is fulfilled. Formally we require the integrated absolute mean velocity anomaly, i.e., the difference between 1 min average values and the 15 min mean, and integrated absolute r.m.s. velocity anomaly are both less than 2.5 times the values inferred identically from a Gaussian white noise of amplitude $u_n = 2\times10^{-2}$ m s^{-1} (instrument noise level). Because the Gaussian synthetic time series can differ for a given realization, we repeat the calculation 1000 times and use the average value. The 2.5 threshold is obtained by conducting similar analysis from unstationary synthetic time series with wave behavior or an imposed significant trend. Another concern for turbulence measurements is when the mean flow changes direction throughout the segment (again violating the stationarity assumption) and, in severe conditions, approaches the TIC from behind the sensors leading to sampling of unnatural turbulence at the wake of the flow. To exclude such segments, we require that the direction of the horizontal current should not deviate more than $\pm60^{\circ}$ from the main streamwise direction over a 15 min segment.

Swell is encountered in parts of the observations, notably toward the end of Floe 4, in relative proximity to the ice edge. Although fluxes measured during swell may be an interesting topic themselves, we chose to exclude these data from the present analysis. Careful analysis is needed to account for the wave orbital velocities and wave-related (nonturbulent) contribution to stress. The period of the swell was approximately 10 s. In order to identify swell, each segment is band-passed between 7 and 20 s, and the turbulence intensity in this range is compared to the turbulence intensity of the unfiltered data. We require that turbulence intensity for the raw data, $I_0 = \sqrt{\frac{1}{3}(u_{rms}^2 + v_{rms}^2 + w_{rms}^2)}$, is significantly greater than that of the band-passed, I_{BP}. Next we require I_{BP} to be sufficiently weak compared to the mean current velocity, $\bar{U}$, and the instrument noise u_n. Formally, we require that

$$\begin{aligned} I_0/I_{BP} &> 1.8, \\ \bar{U}/I_{BP} &> 1.8, \\ I_{BP} &< 4 \times u_n. \end{aligned} \tag{A3}$$

Together, these criteria are found to effectively flag segments where the assumptions for eddy covariance measurement of turbulence are suspect, noise or swell contaminates our measurements. Exact rejection limits are ad hoc, to ensure effective flagging of bad data while retaining good data.

A4. Covariance Segment Length

The choice of 15 min intervals is based on experience from numerous experiments [*McPhee*, 2008], and is a balance between capturing all the true covariance from turbulent eddies and avoiding longer term temporal changes.

The rapid melt in spring stratifies the otherwise typically well-mixed layer, resulting in increasing buoyancy frequency. Extra care must be taken if buoyancy frequency approaches our measurement interval of 15 min. We calculate the buoyancy frequency of the upper 6 m using the microstructure profiler data [*Meyer et al.*, 2016]. Typical buoyancy period is approximately 1 h (or less, i.e., well-mixed), but in June periods of 10 min and less are observed. During periods of short buoyancy periods, internal waves may affect the turbulent fluxes inferred using 15 min segments. Recalculations of turbulent heat fluxes using segment length down to 5 min, however, reveal no significant difference from 15 min segments. Any segments violating Taylor's hypothesis are already flagged by our systematic procedure, and we consider the remaining data of acceptable quality. To be consistent throughout, we retain 15 min calculations for the entire data set.

Acknowledgments
The field work has been supported by the Norwegian Polar Institute's Centre for Ice, Climate and Ecosystems (ICE) through the N-ICE project. Additional support was obtained from the Centre for Climate Dynamics at the Bjerknes Centre through grant BASIC: Boundary Layers in the Arctic Atmosphere, Seas and Ice Dynamics. AKP is supported by the Research Council of Norway, through the project 229786. AR's work was supported through the project "Carbon Bridge," a Polar Program (project 226415) funded by the Norwegian Research Council. We thank everyone involved in the field campaign for making this study possible. The comments from two reviewers helped clarifying and improving the manuscript. The following data sets were used in this study and are publicly available at the Norwegian Polar Data Centre: TIC data [*Peterson et al*., 2016], microstructure sonde (MSS) [*Meyer et al*., 2016], meteorological data [*Hudson et al*., 2015], and ice thickness from hot wires [*Rösel et al*., 2016].

References

Assmy, P., et al. (2017), Leads in arctic pack ice enable early phytoplankton blooms below snow-covered sea ice, *Sci. Rep.*, *7*, 40850, doi:10.1038/srep40850.
Carmack, E. C., et al. (2015), Toward quantifying the increasing role of oceanic heat in sea ice loss in the new Arctic, *Bull. Am. Meteorol. Soc.*, *96*(12), 2079–2105, doi:10.1175/BAMS-D-13-00177.1.
Cole, S. T., M.-L. Timmermans, J. M. Toole, R. A. Krishfield, and F. T. Thwaites (2014), Ekman veering, internal waves, and turbulence observed under Arctic sea ice, *J. Phys. Oceanogr.*, *44*(5), 1306–1328, doi:10.1175/JPO-D-12-0191.1.
Fer, I. (2009), Weak vertical diffusion allows maintenance of cold halocline in the central Arctic, *Atmos. Ocean Sci. Lett.*, *2*(3), 148–152, doi:10.1080/16742834.2009.11446789.
Fer, I. (2014), Near-inertial mixing in the central Arctic Ocean, *J. Phys. Oceanogr.*, *44*(8), 2031–2049, doi:10.1175/JPO-D-13-0133.1.
Fer, I., M. Müller, and A. K. Peterson (2015), Tidal forcing, energetics, and mixing near the Yermak Plateau, *Ocean Sci.*, *11*(2), 287–304, doi:10.5194/os-11-287-2015.
Fer, I., A. K. Peterson, A. Meyer, and A. Randelhoff (2017), One-dimensional evolution of the upper water column in the Atlantic sector of the Arctic Ocean in winter, *J. Geophys. Res. Oceans*, doi:10.1002/2016JC012431, in press.
Gallaher, S. G., T. P. Stanton, W. J. Shaw, S. T. Cole, J. M. Toole, J. P. Wilkinson, T. Maksym, and B. Hwang (2016), Evolution of a Canada Basin ice-ocean boundary layer and mixed layer across a developing thermodynamically forced marginal ice zone, *J. Geophys. Res. Oceans*, *121*, 6223–6250, doi:10.1002/2016JC011778.
Granskog, M., P. Assmy, S. Gerland, G. Spreen, H. Steen, and L. H. Smedsrud (2016), Arctic research on thin ice: Consequences of Arctic sea ice loss, *Eos*, *97*, doi:10.1029/2016EO044097.
Hudson, S. R., M. A. Granskog, A. Sundfjord, A. Randelhoff, A. H. H. Renner, and D. V. Divine (2013), Energy budget of first-year Arctic sea ice in advanced stages of melt, *Geophys. Res. Lett.*, *40*, 2679–2683, doi:10.1002/grl.50517.
Hudson, S. R., L. Cohen, and V. Walden (2015), N-ICE2015 surface meteorology v2, Norwegian Polar Inst., doi:10.21334/npolar.2015.056a61d1.
Itkin, P., G. Spreen, S. R. Hudson, B. Cheng, M. Doble, N. Sennechael, C. Provost, J. Haapala, M. Nikolaus, L. Kaleschke, and J. Wilkinson (2015), N-ICE2015 buoy data, Norwegian Polar Inst., doi:10.21334/npolar.2015.6ed9a8ca.
Jeffries, M. O., J. E. Overland, and D. K. Perovich (2013), The Arctic shifts to a new normal, *Phys. Today*, *66*(10), 35, doi:10.1063/PT.3.2147.
Krishfield, R. A., A. Proshutinsky, K. Tateyama, W. J. Williams, E. C. Carmack, F. A. McLaughlin, and M.-L. Timmermans (2014), Deterioration of perennial sea ice in the Beaufort Gyre from 2003 to 2012 and its impact on the oceanic freshwater cycle, *J. Geophys. Res. Oceans*, *119*, 1271–1305, doi:10.1002/2013JC008999.
Lindsay, R., and A. Schweiger (2015), Arctic sea ice thickness loss determined using subsurface, aircraft, and satellite observations, *Cryosphere*, *9*(1), 269–283, doi:10.5194/tc-9-269-2015.
Maykut, G. A., and M. G. McPhee (1995), Solar heating of the Arctic mixed layer, *J. Geophys. Res.*, *100*(C12), 24,691–24,703, doi:10.1029/95JC02554.
McPhee, M. G. (1988), Analysis and prediction of short-term ice drift, *J. Offshore Mech. Arctic Eng.*, *110*(1), 94–100, doi:10.1115/1.3257130.
McPhee, M. G. (1992), Turbulent heat flux in the upper ocean under sea ice, *J. Geophys. Res.*, *97*(C4), 5365–5379, doi:10.1029/92JC00239.
McPhee, M. G. (1994), On the turbulent mixing length in the oceanic boundary layer, *J. Phys. Oceanogr.*, *24*(9), 2014–2031, doi:10.1175/1520-0485(1994)024¡2014:OTTMLI¿2.0.CO;2.
McPhee, M. G. (2002), Turbulent stress at the ice/ocean interface and bottom surface hydraulic roughness during the SHEBA drift, *J. Geophys. Res.*, *107*(C10), 8037, doi:10.1029/2000JC000633.
McPhee, M. G. (2008), *Air-Ice-Ocean Interaction: Turbulent Ocean Boundary Layer Exchange Processes*, pp. 1–215, Springer, New York, doi:10.1007/978-0-387-78335-2.
McPhee, M. G., G. A. Maykut, and J. H. Morison (1987), Dynamics and thermodynamics of the ice/upper ocean system in the marginal ice zone of the Greenland Sea, *J. Geophys. Res.*, *92*(C7), 7017–7031, doi:10.1029/JC092iC07p07017.
McPhee, M. G., T. Kikuchi, J. H. Morison, and T. P. Stanton (2003), Ocean-to-ice heat flux at the North Pole environmental observatory, *Geophys. Res. Lett.*, *30*(24), 2274, doi:10.1029/2003GL018580.
McPhee, M. G., R. Kwok, and R. Robins (2005), Upwelling of Arctic pycnocline associated with shear motion of sea ice, *Geophys. Res. Lett.*, *32*, L10616, doi:10.1029/2004GL021819.
McPhee, M. G., J. H. Morison, and F. Nilsen (2008), Revisiting heat and salt exchange at the ice-ocean interface: Ocean flux and modeling considerations, *J. Geophys. Res.*, *113*, C06014, doi:10.1029/2007JC004383.
Meyer, A., et al. (2017), Winter to summer oceanographic observations in the Arctic Ocean north of Svalbard, *J. Geophys. Res. Oceans.*, doi:10.1002/2016JC012391, in press.
Meyer, A., et al. (2016), N-ICE2015 ocean microstructure profiles (MSS90L), Norwegian Polar Inst., doi:10.21334/npolar.2016.774bf6ab.
Morison, J. H., M. G. McPhee, and G. A. Maykut (1987), Boundary layer, upper ocean, and ice observations in the Greenland Sea Marginal Ice Zone, *J. Geophys. Res.*, *92*(C7), 6987–7011, doi:10.1029/JC092iC07p06987.
Notz, D., M. G. McPhee, M. G. Worster, G. A. Maykut, K. H. Schlünzen, and H. Eicken (2003), Impact of underwater-ice evolution on Arctic summer sea ice, *J. Geophys. Res.*, *108*(C7), 3223, doi:10.1029/2001JC001173.
Onarheim, I. H., L. H. Smedsrud, R. B. Ingvaldsen, and F. Nilsen (2014), Loss of sea ice during winter north of Svalbard, *Tellus, Ser. A*, *66*(1), 1–9, doi:10.3402/tellusa.v66.23933.
Padman, L., and S. Erofeeva (2004), A barotropic inverse tidal model for the Arctic Ocean, *Geophys. Res. Lett.*, *31*, L02303, doi:10.1029/2003GL019003.
Padman, L., A. J. Plueddemann, R. D. Muench, and R. Pinkel (1992), Diurnal tides near the Yermak Plateau, *J. Geophys. Res.*, *97*(C8), 12,639–12,652, doi:10.1029/92JC01097.
Peterson, A. K., I. Fer, A. Randelhoff, A. Meyer, L. Håvik, L. H. Smedsrud, I. Onarheim, M. Muijlwick, A. Sundfjord, and M. G. McPhee (2016), N-ICE2015 ocean turbulent fluxes from under-ice turbulent cluster, Norwegian Polar Inst., doi:10.21334/npolar.2016.ab29f1e2.
Rainville, L., C. Lee, and R. Woodgate (2011), Impact of wind-driven mixing in the Arctic Ocean, *Oceanography*, *24*(3), 136–145, doi:10.5670/oceanog.2011.65.
Randelhoff, A., A. Sundfjord, and A. H. H. Renner (2014), Effects of a shallow pycnocline and surface meltwater on sea ice-ocean drag and turbulent heat flux, *J. Phys. Oceanogr.*, *44*(8), 2176–2190, doi:10.1175/JPO-D-13-0231.1.
Rösel, A., et al. (2016), N-ICE2015 ice thickness from hot wires, Norwegian Polar Inst., doi:10.21334/npolar.2016.263a317f.
Rudels, B., R. Meyer, E. Fahrbach, V. V. Ivanov, S. Østerhus, D. Quadfasel, U. Schauer, V. Tverberg, and R. A. Woodgate (2000), Water mass distribution in Fram Strait and over the Yermak Plateau in summer 1997, *Ann. Geophys.*, *18*(6), 0687–0705, doi:10.1007/s005850000216.
Rudels, B., E. P. Jones, U. Schauer, and P. Eriksson (2004), Atlantic sources of the Arctic Ocean surface and halocline waters, *Polar Res.*, *23*(2), 181–208, doi:10.1111/j.1751-8369.2004.tb00007.x.

Serreze, M. C., and J. C. Stroeve (2015), Arctic sea ice trends, variability and implications for seasonal ice forecasting, *Philos. Trans. R. Soc. A*, *373*(2045), 1–16, doi:10.1098/rsta.2014.0159.

Shaw, W. J., T. P. Stanton, M. G. McPhee, and T. Kikuchi (2008), Estimates of surface roughness length in heterogeneous under-ice boundary layers, *J. Geophys. Res.*, *113*, C08030, doi:10.1029/2007JC004550.

Shaw, W. J., T. P. Stanton, M. G. McPhee, J. H. Morison, and D. G. Martinson (2009), Role of the upper ocean in the energy budget of Arctic sea ice during SHEBA, *J. Geophys. Res.*, *114*, C06012, doi:10.1029/2008JC004991.

Sirevaag, A. (2009), Turbulent exchange coefficients for the ice/ocean interface in case of rapid melting, *Geophys. Res. Lett.*, *36*, L04606, doi:10.1029/2008GL036587.

Sirevaag, A., and I. Fer (2009), Early spring oceanic heat fluxes and mixing observed from drift stations north of Svalbard, *J. Phys. Oceanogr.*, *39*(12), 3049–3069, doi:10.1175/2009JPO4172.1.

Stanton, T. P., W. J. Shaw, and J. K. Hutchings (2012), Observational study of relationships between incoming radiation, open water fraction, and ocean-to-ice heat flux in the Transpolar Drift: 2002-2010, *J. Geophys. Res.*, *117*, C07005, doi:10.1029/2011JC007871.

Stroeve, J. C., M. C. Serreze, M. M. Holland, J. E. Kay, J. Malanik, and A. P. Barrett (2012), The Arctic's rapidly shrinking sea ice cover: A research synthesis, *Clim. Change*, *110*(3–4), 1005–1027, doi:10.1007/s10584-011-0101-1.

Taskjelle, T., M. A. Granskog, A. K. Pavlov, S. R. Hudson, and B. Hamre (2016), Effects of an Arctic under-ice bloom on solar radiant heating of the water column, *J. Geophys. Res. Oceans*, doi:10.1002/2016JC012187, in press.

Thorpe, S. A. (2007), *An Introduction to Ocean Turbulence*, Cambridge Univ. Press, Cambridge, U. K.

Tietsche, S., D. Notz, J. H. Jungclaus, and J. Marotzke (2011), Recovery mechanisms of Arctic summer sea ice, *Geophys. Res. Lett.*, *38*, L02707, doi:10.1029/2010GL045698.